


A Stretchable Terahertz Parabolic-Shaped Metamaterial

Zefeng Xu and Yu-Sheng Lin*

A stretchable parabolic-shaped metamaterial (PSM) coated onto polydimethylsiloxane (PDMS) is proposed and demonstrated for operation in the terahertz (THz) frequency range. By stretching the PDMS-based PSM device along different directions, ultranarrowband, polarization dependent, switchable optical characteristics are obtained. By stretching the PSM width and length in the transverse electric (TE) and transverse magnetic (TM) modes, resonant tuning ranges of 0.55 and 0.32 THz, respectively, are demonstrated for the PSM device. In these deformation ranges, the *Q*-factors of the PSM device for different widths and lengths are quite stable and maintained in the range of 9 to 14 for the TE mode, with a high *Q*-factor of 50 obtained at resonance for the TM mode. The integration of the PSM on a mechanically deformable PDMS substrate provides potential for use in flexible electronics applications. Furthermore, the PSM device exhibits single-/dual-band switching and polarization switching characteristics. These multifunctional states for the PSM device can be determined by mechanical inputs to represent binary digits that can then be used to perform logic operations. Such a stretchable PSM device offers an effective approach for the realization of programmable metamaterials with enhanced optical-mechanical performance due to its high flexibility, applicability, and cost-effectiveness.

The terahertz (THz) wave is an electromagnetic wave occurring in the frequency range from 0.1 to 10 THz that was officially named in the late 1980s.^[1] THz waves have become an emerging field in science and technology because of the extraordinary characteristics of these waves, which are safe for biological tissues, show high transmission for common plastics, and show a higher spatial resolution for optical and imaging system applications. Recently, research has been driven by these extraordinary characteristics of THz waves in physics studies, security imaging, nondestructive testing, explosive detection, wireless communication, chemical analysis, and molecule identification.^[2] Integrated THz optics can be composed of miniaturized optical components to enhance the transmission or reflection.^[3] This miniaturization allows for high-density compact systems and enables integration with other systems for increasing flexibility and applicability.

Z. Xu, Prof. Y.-S. Lin
State Key Laboratory of Optoelectronic Materials and Technologies
School of Electronics and Information Technology
Sun Yat-Sen University
Guangzhou 510275, China
E-mail: linyoush@mail.sysu.edu.cn

 The ORCID identification number(s) for the author(s) of this article can be found under <https://doi.org/10.1002/adom.201900379>.

DOI: 10.1002/adom.201900379

For example, a THz device can be compacted into semiconductor and photonic integrated circuits.^[4] Such miniaturized THz optical components require new techniques and approaches, especially for actively tunable and multifunctional THz devices. In addition, the polarization-dependent characteristic is a key optical property of a THz wave when utilized for security, THz imaging, and digital information applications.^[5–7]

A metamaterial is a composite material that possesses extraordinary electromagnetic properties realized by the configuration of specific structures. Metamaterials have attracted broad attention over the past few decades.^[8] Typical metamaterials are “left-hand materials,” “photonic crystals,” and “supermagnetic materials,”^[9] which are composed of artificial “atoms” having some unique properties.^[10] By designing and arranging artificial atoms and molecular units, a metamaterial can be made to show various optical properties. Among the entire electromagnetic spectrum, a metamaterial is a feasible

material for use in optoelectronics applications in the THz frequency range. Transformation optics is one of the key theories to describe the propagation path of an electromagnetic wave.^[11] The propagation path has been demonstrated on a theoretical level. There have been many novel inventions that have been greatly improved by using a THz metamaterial to replace classic devices, such as waveguides, resonators, filters, polarizers, and switches.^[12–16] To make a THz metamaterial more flexible and applicable, some progress has been made in the realization of controlling THz waves by using optical,^[17] electrical,^[18] magnetic,^[19] and thermal^[20–23] approaches. Among these approaches, a reconfigurable metamaterial becomes feasible in the active manipulation of THz wave applications. This manipulation can be achieved by reconfiguring the geometrical dimension of a metamaterial,^[24–26] reforming the structure,^[27–31] and bending the substrate or lattice.^[32,33] The geometrical variations of the metamaterial are mostly generated from the mechanical movement or deformation within metamaterial structures.^[34,35] These reconfigurable and reformable metamaterials can be actively tuned by electrical, magnetic, thermal, and optical approaches. However, these approaches are limited to certain applications owing to symmetric or asymmetric split-ring resonator configurations. Moreover, tunable THz metamaterials reported in the literature are limited to low *Q*-factors (≈ 0.5 –5) and require complicated fabrication processes.^[36–38] Meanwhile, fabrication is mostly completed

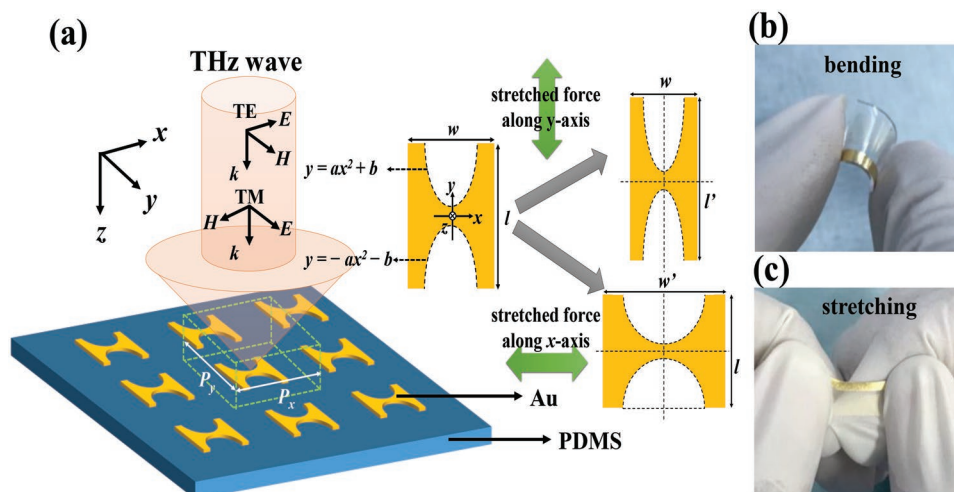


Figure 1. a) Schematic illustrations of the proposed PSM device operated by applying a stretching force along the x- and y-axis directions. b,c) Photographs of the PSM fabricated on a PDMS substrate, which show its flexibility.

on Si, III–V materials, and quartz substrates, which strictly limits their possible applications, such as applications that have a requirement for a curved surface. For boosting the manufacturing and testing processes, a tunable metamaterial controlled by a loading mechanical force becomes an alternative approach.^[27] In view of these points, the requirement of a multifunctional THz device with a high Q -factor and actively tunable resonance turns into a hot research topic for scientists.

To enhance the performance of electromagnetic characteristics and improve the resonant tuning range, we demonstrate a mechanical approach based on deforming a flexible substrate to tune the resonance of a THz metamaterial. The tunable approach for metamaterials using flexible substrates has been reported previously, including the use of polyimide (PI), polyethylene naphthalene (PEN), polyethylene terephthalate (PET), Kapton, and polydimethylsiloxane (PDMS).^[39–41] In all of these flexible materials, PDMS is a commonly used flexible substrate owing to the properties of tear resistance, electrical insulation, low electrical losses, full permeability, and good ductility in the THz frequency range.^[29] PDMS-based substrates possess great advantages in terms of conformable manipulation, flexibility, biocompatibility, transparency, portability, and low-cost compared to flat and rigid substrates, e.g., quartz and silicon. Therefore, the integration of a high-efficiency THz metamaterial on a flexible PDMS substrate can better leverage the advantages of the metamaterial and provide significant prospects in flexible optoelectronics. In this study, an active tuning approach for a THz metamaterial with an ultranarrow bandwidth is presented. The proposed device exhibits a larger scalability, higher polarization dependence, and larger tuning range compared to devices reported in the literature.^[24–35,42–50] Owing to the low stiffness with large proof mass of the PDMS-based metamaterial, one can generate a large deformation by applying a small strain force. Therefore, a high-efficiency switch modulation with ultrahigh Q -factor can be realized. This device structure exhibits a resonant tuning range of 0.45 THz with a high Q -factor of 50 under a deformation quantity of 60 μm along a 1D direction. These results are better than those reported in

the literature.^[15,24–34,51–53] Furthermore, the proposed device exhibits the multifunctionalities of a large tunability and p/s-polarization switching, i.e., transverse magnetic (TM)/transverse electric (TE) switching. Such a design provides potential possibilities for use in biomedical imaging, active sensors, modulators, and flexible electronics applications.

Figure 1a presents schematic illustrations of the proposed stretchable THz metamaterial device, which is composed of an asymmetric parabolic-shaped metamaterial (PSM). The pattern of the PSM device follows a quadratic function expressed by the equation $y = \pm ax^2 \pm b$, where a and b are coefficients of the quadratic function. The fabrication process for the PSM device is started by the deposition of an Au layer on a PDMS elastic substrate. The thickness of the Au layer is 100 nm. The geometrical deformation for a device under the application of a stretching force along the x- and y-axis directions is also presented in Figure 1a. The incident light is normally propagated along the z-axis direction, where k is the wavevector of the incident THz wave. Herein, the stretchable force applied to the PSM device along the x- and y-axis directions can be expressed by Equations (1) and (2) for the deformations of a PSM with width (w) and length (l), respectively

$$\varepsilon_x = \sigma_x / E \quad (1)$$

$$\varepsilon_y = \sigma_y / E \quad (2)$$

where ε_x and ε_y are the proportions of the length changes with respect to the initial lengths, σ_x and σ_y are the strain forces applied to the PDMS along the x- and y-axis directions, respectively, and E is Young's modulus of PDMS. The resonant frequency of the proposed PSM device is a function of the effective refractive index of a THz wave referring to the theory of the Drude–Lorentz model,^[27] i.e., $n_{\text{eff}} = \sqrt{\mu_{\text{eff}} \varepsilon_{\text{eff}}}$, where μ_{eff} and ε_{eff} are the effective permeability and permittivity of the PSM, respectively. The optical impedance (Z) can be calculated by Equation (3)^[54]

$$Z = \pm \sqrt{\frac{(1+r)^2 - t^2}{(1-r)^2 - t^2}} \quad (3)$$

where t is the transmission coefficient and r is the reflection coefficient. The corresponding imaginary and real parts of the refraction index (n_{eff}) can be expressed by Equations (4) and (5),^[55] respectively

$$\text{Im}(n_{\text{eff}}) = \pm \text{Im} \left\{ \frac{\cos^{-1} \left[\frac{1}{2t} (1 - r^2 + t^2) \right]}{kd} \right\} \quad (4)$$

$$\text{Re}(n_{\text{eff}}) = \pm \text{Re} \left\{ \frac{\cos^{-1} \left[\frac{1}{2t} (1 - r^2 + t^2) \right]}{kd} \right\} + \frac{2m\pi}{kd} \quad (5)$$

where k is the incident wavevector, m is an integer, and d is the PSM thickness. The values for μ_{eff} and ϵ_{eff} can be found by

using $\mu_{\text{eff}} = n_{\text{eff}} Z$ and $\epsilon_{\text{eff}} = n_{\text{eff}} / Z$. The approximated capacitance (C) between adjacent metamaterial resonators can be calculated by using Equation (6)

$$C = \frac{\varphi \epsilon_0 \epsilon_d w d}{P - l} \quad (6)$$

where ϵ_0 is the permittivity in free space, ϵ_d is the relative permittivity, φ is a factor that numerically approximates the nonuniform charge distribution, w is the PSM width, l is the PSM length, P is the PSM period, and d is the PSM thickness, respectively. In this study, d is the thickness of the Au layer, which is kept as a constant value of 100 nm, and P is defined initially as a constant value of 60 μm ($P = P_x = P_y = 60 \mu\text{m}$). The initial pattern of the PSM is 30 $\mu\text{m} \times 30 \mu\text{m}$ ($w \times l$). Therefore, the active tunabilities of the PSM device can be achieved by applying a stretch force to change the w value and l value along the x - and y -axis directions, respectively, i.e., deforming P_x and P_y , respectively. Figure 1b,c shows photographs of a PSM fabricated on a PDMS substrate, which demonstrate its flexibility.

The transmittance of the PSM device with different a values for the TE and TM modes is presented in Figure 2.

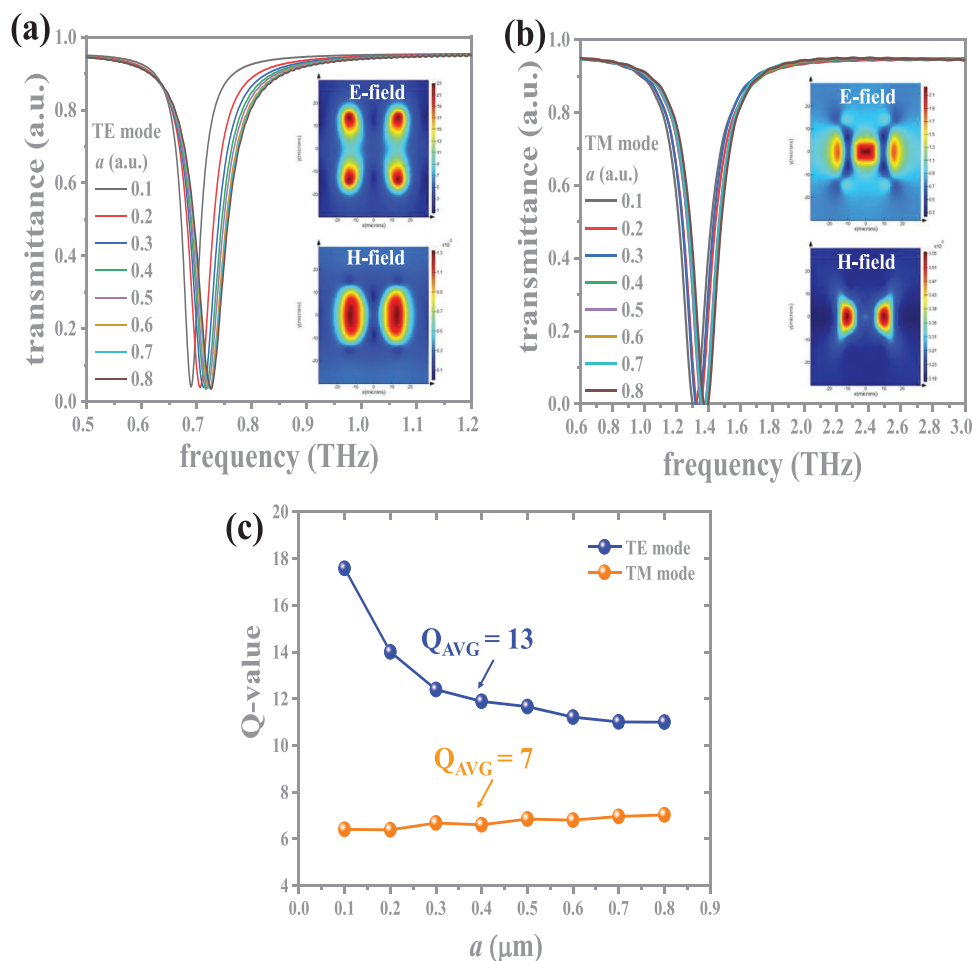


Figure 2. Transmittance of a PSM device with different a values in the a) TE mode and b) TM mode. The corresponding E- and H-field distributions of the PSM device with $a = 0.1$ in the TE and TM modes are shown in the inserted images of (a,b), respectively. c) The relationships between the Q-factors and a values in the TE and TM modes.

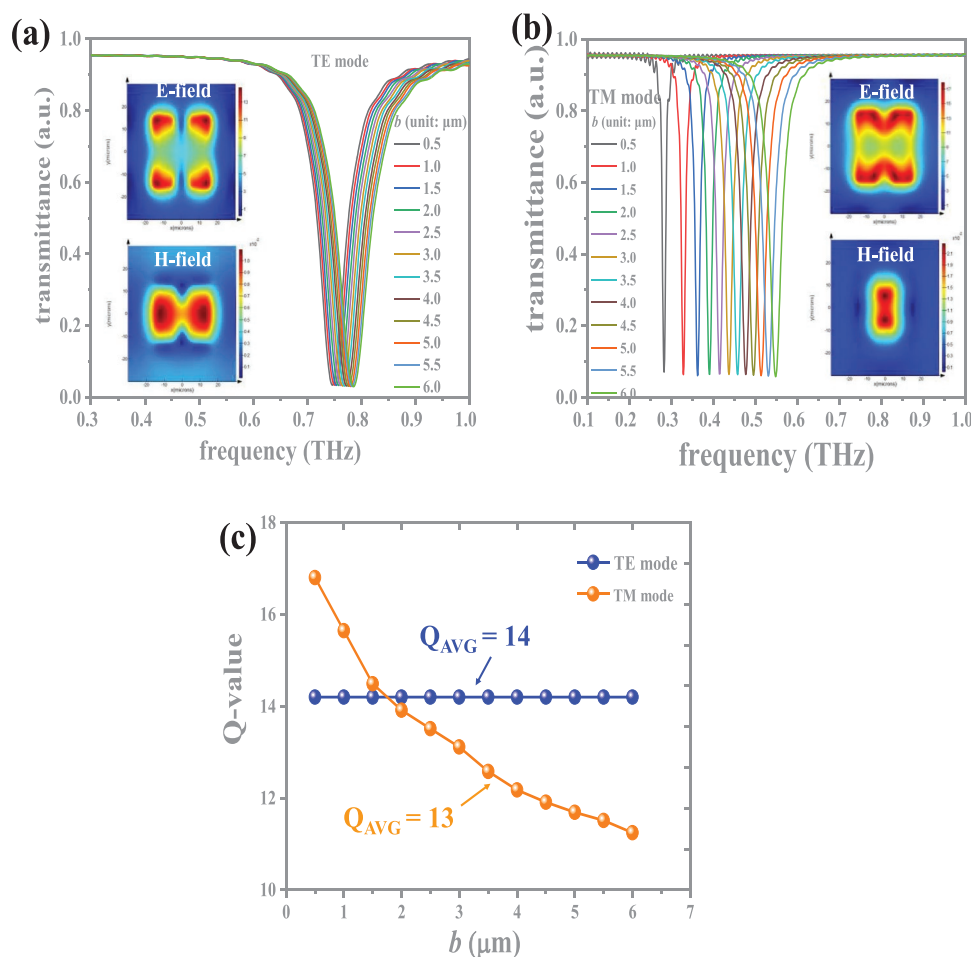


Figure 3. Transmittance of a PSM device with different b values in the a) TE mode and b) TM mode. The corresponding E- and H-field distributions of the PSM device with $b = 6.0$ in the TE and TM modes are shown in the inserted images of (a,b), respectively. c) The relationships between the Q -factors and b values in the TE and TM modes.

In the TE mode, the transmittance is maintained at 96% by varying the value of a from 0.1 to 0.8, as shown in Figure 2a. By increasing the value of a , the resonance is blueshifted by 0.06 THz, and the corresponding Q -factor is defined as the resonance divided by the full-width at half-maximum (FWHM) bandwidth, which decreases exponentially and reaches a stable state with an average Q -factor of 13, as indicated as the blue curve in Figure 2c. In the TM mode, the transmittance is blueshifted by 0.10 THz by varying a from 0.1 to 0.8, as shown in Figure 2b. The corresponding Q -factors are identical with an average value of 7. This result shows that the resonance is very stable in the TM mode. The E- and H-field distributions for the PSM with different values for a in the TE and TM modes are shown in the inserted images of Figure 2a,b, respectively. It can be observed that the E-field energy is mainly distributed on the four apexes of the PSM, while the H-field energy is mainly concentrated on both sides of the H-shape of the PSM in the TE mode. In the TM mode, the incident THz wave is rotated by 90° compared to that in the TE mode. Most of the E-field energy is distributed in the central region of the PSM, while the H-field energy remains on both sides of the H-shape of the PSM.

Figure 3 presents the transmittance for a PSM device with different b values in the TE and TM modes. The resonances are substantially kept at 96% in the TE mode by varying b from 0.5 to 6.0, as shown in Figure 3a. By increasing b , the resonance is blueshifted by 0.04 THz, and the corresponding Q -factor is 14, as shown by the blue curve in Figure 3c. In the TM mode, the resonance is blueshifted by 0.28 THz by varying b from 0.5 to 6.0, as shown in Figure 3b. The corresponding Q -factor decreases exponentially and reaches a stable state with an average Q -factor of 13, as shown by the orange curve in Figure 3c. This result shows that the varying resonance is very stable in the TE mode. The E- and H-field distributions for the PSM with different b values in the TE and TM modes are shown in the inserted images of Figure 3a,b, respectively. It is obviously observed that the E-field energy is mainly distributed on the four apexes of the PSM, while the H-field energy is mainly concentrated on both sides of the H-shape of the PSM in the TE mode. In the TM mode, most of the E-field energy is distributed around the contour of the PSM, while the H-field energy is concentrated on the center of the PSM.

The transmittance of the PSM device with different w values in the TE and TM modes is shown in **Figure 4**.

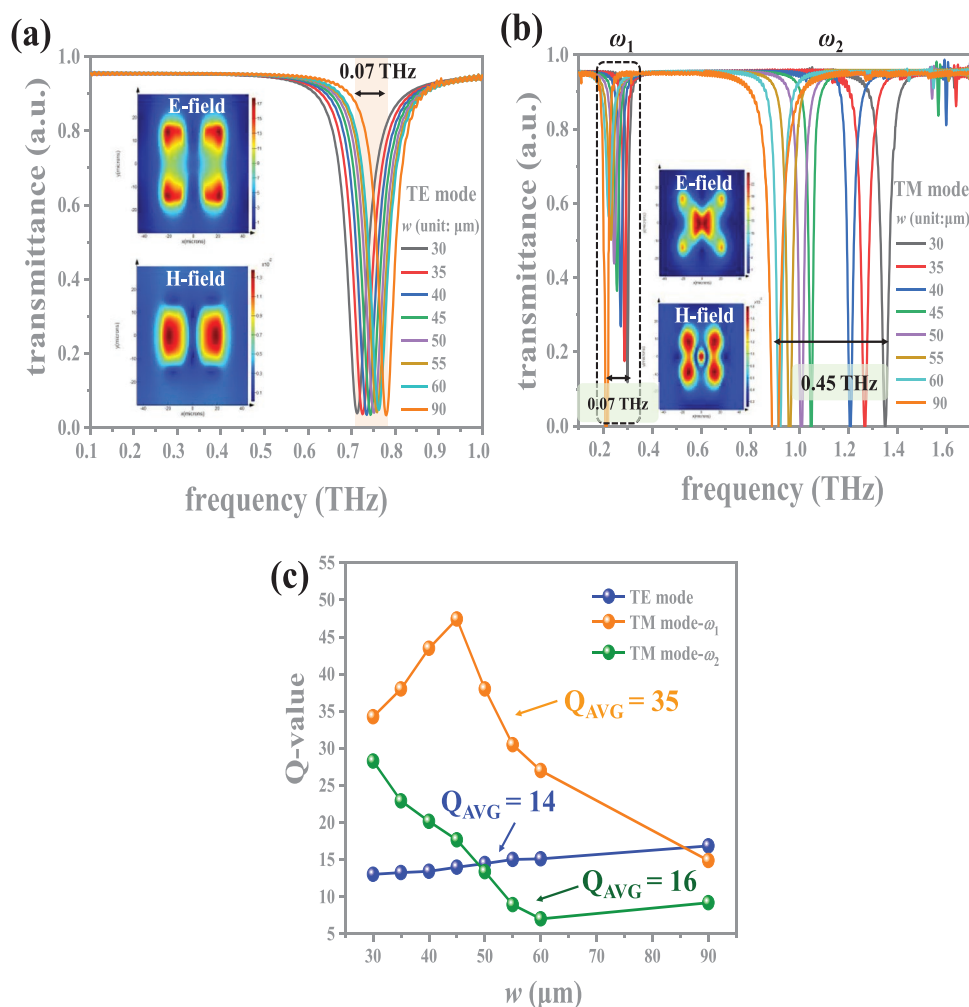


Figure 4. Transmittance of a PSM device with different w values in the a) TE mode and b) TM mode. The corresponding E- and H-field distributions of the PSM device with $w = 45 \mu\text{m}$ in the TE and TM modes are shown in the inserted images of (a,b), respectively. c) The relationships between the Q -factors and w values in the TE and TM modes.

The variation in the value of w is caused by the stretching of the PSM device along the x -axis direction by keeping the PSM length (l) constant at $30 \mu\text{m}$ owing to the sharp reduction in the Poisson ratio of PDMS during the O_2 plasma process. The longitudinal strain (along the y -axis direction) can be ignored. In the initial state, i.e., $w = 30 \mu\text{m}$ and $l = 30 \mu\text{m}$, the resonance can be tuned by 0.07 THz by stretching the PSM device from $w = 30 \mu\text{m}$ to $w = 90 \mu\text{m}$ in the TE mode, as presented in Figure 4a. The corresponding Q -factor is quite linear with an average value of 14, as shown by the blue curve in Figure 4c. In the TM mode, two resonances are generated: an electric quadrupole mode at 0.30 THz for the first resonance and a dipole mode at 1.35 THz for the second resonance, which are denoted as ω_1 and ω_2 , respectively, as shown in Figure 4b. By stretching the PSM device, i.e., increasing the w value, two resonances are redshifted with tuning ranges of 0.07 and 0.45 THz from $w = 30 \mu\text{m}$ to $w = 90 \mu\text{m}$, respectively. This large tuning range of 0.45 THz is due to the change of the PSM period along the x -axis direction. This change can be explained by Equation (7)^[56,57]

$$\lambda_a = \frac{P_x P_y}{\sqrt{i^2 P_y^2 + j^2 P_x^2}} \sqrt{\frac{\epsilon_m \epsilon_d}{\epsilon_m + \epsilon_d}} \quad (7)$$

where ϵ_m is the permittivity of the metal, ϵ_d is the permittivity of the dielectric, P_x is the PSM period along the x -axis direction, P_y is the PSM period along the y -axis direction, and i and j are integers, respectively. Therefore, the resonance is determined by the PSM period. The corresponding Q -factor decreases linearly with an average value of 16, as shown by the green curve in Figure 4c. For the electric quadrupole resonance, the trend for the corresponding Q -factor increases linearly in the deformation range of $w = 30 \mu\text{m}$ to $w = 45 \mu\text{m}$ before reaching a maximum Q -factor of 47. When the deformation w value is larger than $45 \mu\text{m}$, the trend for the Q -factor decreases exponentially with an average Q -factor of 35, as indicated by the orange curve in Figure 4c. The inserted images in Figure 4a,b show the corresponding E- and H-field distributions. The E-field energy is mainly distributed on the four apexes of the PSM, and the H-field energy is mainly concentrated on both

sides of the H-shape of the PSM in the TE mode. In the TM mode, the E-field energy is distributed on the four corners of the PSM and most of the energy is concentrated on the center of the PSM. Conversely, most of the H-field energy is concentrated on the four apexes of the PSM, which is stronger than that at the center of the PSM. A summary of the Q -factors and w variations are plotted in Figure 4c. This graph shows the distinctive pathways of the resonances for a certain w value when exhibiting similar hysteresis behavior, which can be observed in natural materials with a phase change characteristic.^[58] Here, this similar hysteresis behavior indicates two stable output states observed by one input control signal. There exists a closed loop for the Q -factor generated by the stretching w value to signify the multifunctional states in the optical-mechanical characteristics of the PSM device. These multifunctional states are artificially created by the induced anisotropic near-field couplings observed in the resonances.

In Figure 5, the transmittance of the PSM device with different l values in the TE and TM modes is presented. The

PSM device is stretched along the y -axis direction, and the PSM width (w) is kept constant at 30 μm owing to the ignored transverse strain (along the x -axis direction) that is realized by reducing the Poisson ratio of the PDMS during the O_2 plasma process. In the TE mode, the resonance is redshifted by 0.32 THz by stretching the l value from 30 to 90 μm , while the resonant intensities of the transmittances can be kept at 80%. The corresponding Q -factor follows a linearly decrease trend before becoming stable with an average Q -factor of 9, as shown by the blue curve in Figure 5d. In the TM mode, two resonances are generated: an electric quadrupole mode at 0.30 THz for the first resonance (ω_1) and a dipole mode at 1.35 THz for the second resonance (ω_2), respectively, as shown in Figure 5b. By stretching the PSM device from $l = 30 \mu\text{m}$ to $l = 90 \mu\text{m}$, two resonances are redshifted with tuning ranges of 0.08 and 0.06 THz, respectively. Although these tuning ranges are quite small, the resonant intensities of the transmittances can be kept as high as 80%. The corresponding average Q -factors of ω_1 and ω_2 are 43 and 30, respectively,

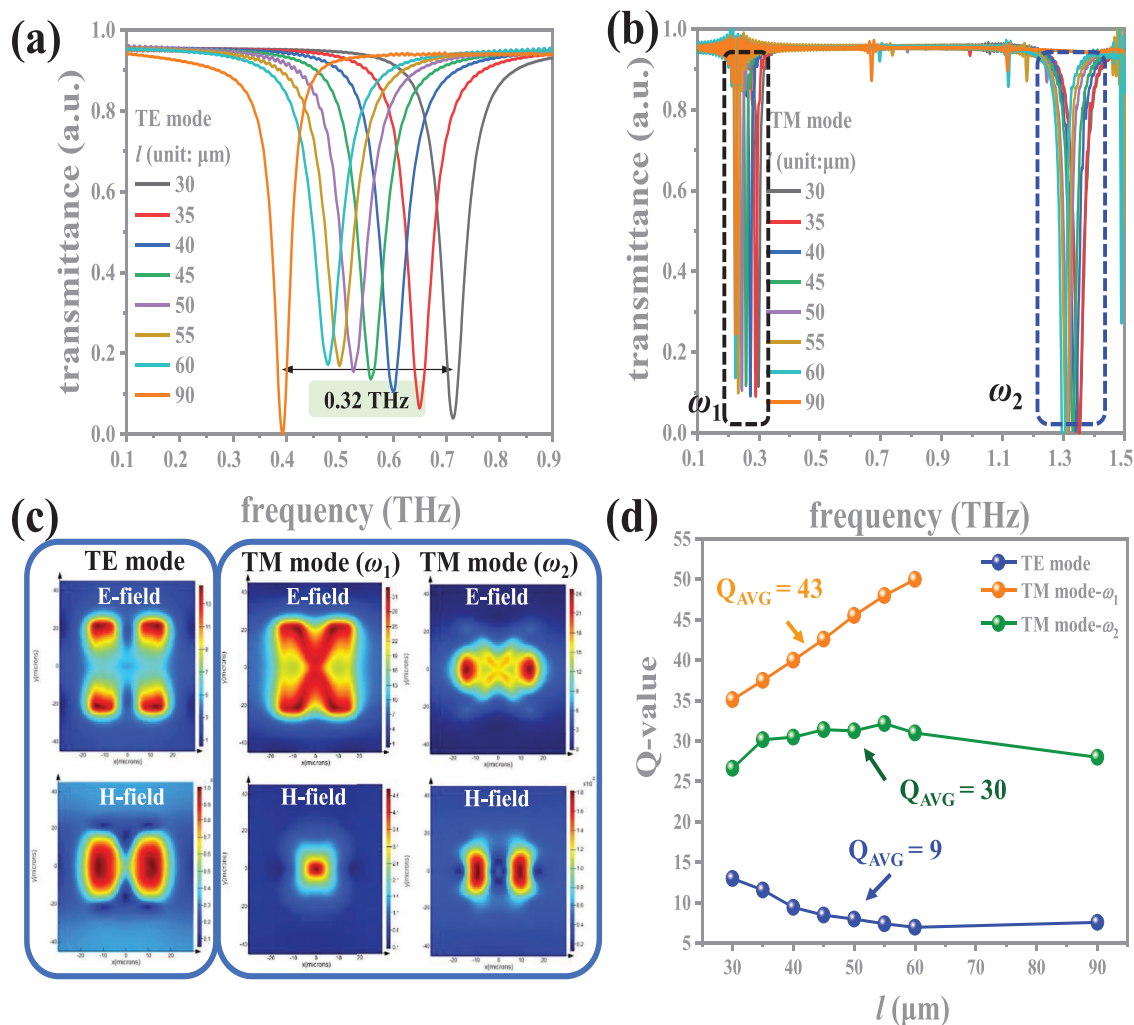


Figure 5. Transmittance of a PSM device with different l values in the a) TE mode and b) TM mode. c) The corresponding E- and H-field distributions of the PSM device with $l = 45 \mu\text{m}$ in the TE and TM modes for the ω_1 and ω_2 resonances. d) The relationships between the Q -factors and l values in the TE and TM modes.

which can be kept stable, as shown by the orange and green curves in Figure 5d. These Q -factors are increased 3.3-fold for ω_1 ($Q_{\text{AVG}} = 43$) and 4.8-fold for ω_2 ($Q_{\text{AVG}} = 30$) compared to the results in the TE mode. It can be observed that the trend of the Q -factor at ω_1 shows a linear increase with a maximum value of 50. The abovementioned electromagnetic performance is better than that obtained for other THz-metamaterial devices reported in the literature.^[17–42,59,60] This result can be explained by the field distributions for the PSM in the TE and TM modes, as shown in Figure 5c. The E-field distribution is distributed on the four apexes of the PSM, and the H-field distribution is mainly concentrated at the center region of the PSM in the TE mode. In the TM mode, the E-field distribution for ω_1 is distributed on the surface of the PSM to form an X-shape electromagnetic response, and the H-field distribution is concentrated on the center region on the PSM surface. Meanwhile, the E- and H-field distributions for ω_2 are complementary with those for ω_1 . To increase the flexibility of the PSM device, the angular sensitivity of the PSM device is a key index for real applications. We further numerically investigate the angular sensitivity of the PSM device. The simulation results for a PSM device stretched along the x - and y -axis directions in the TE and TM modes with different bending angles from 0° to 60° are shown in Figure S1 (Supporting Information). The resonance is shifted within 0.10 THz. This shift indicates that the effect of the bending angle on the transmittance is minor.

Summaries for the experimental results for the relationships of the resonances to the PSM geometrical deformation with different w and l values are plotted in Figure 6. By stretching the w value along the x -axis direction, the resonance is blueshifted by 0.06 THz in the TE mode, and the resonances are redshifted by 0.55 THz in the TM mode, as shown in Figure 6a. By stretching the l value along the y -axis direction, the resonances are redshifted by 0.32 and 0.06 THz in the TE and TM modes, respectively, as presented in Figure 6b. The inserted optical micrograph images in Figure 6a,b show the PSM device stretched along the x - and y -axis directions to deform via double elongations from the initial state ($w = 30 \mu\text{m}$). These results show that the PSM device possesses active tunabilities with

ultranarrowband characteristics, which is in good agreement with preliminary simulation results. This tunability paves the way for using this proposed PSM device in flexible THz wave applications.

To investigate our proposed PSM device with the switching function of s- and p-polarization waves, the polarization characteristics of the device are summarized in Figure 7. By stretching the PSM device along the x -axis direction (varying w value from 30 to 60 μm), the s- and p-polarized spectra are plotted in Figure 7a–d. It is clearly observed that the resonance can be switched between single- and dual-bands with an ultra-high Q -factor. Figure 7e shows a summary of the resonances obtained by stretching the w value. The first resonance (ω_1) is almost identical at 0.30 THz, while the second (ω_2) and third (ω_3) resonances are blueshifted by 0.05 THz and redshifted by 0.46 THz, respectively. The switching range for the s- and p-polarization waves spans from 0.20 to 1.40 THz. By stretching the PSM device along the y -axis direction (varying l value from 30 to 60 μm), the s- and p-polarized spectra are plotted in Figure 7f–i. The resonance for s- and p-polarization is single-band with an ultrahigh Q -factor. Figure 7f shows a summary of the resonances obtained by stretching the l value. The first (ω_1) and second (ω_2) resonances are redshifted by 0.12 and 0.25 THz, respectively. The switching range for s- and p-polarization spans from 0.30 to 0.70 THz. It is worth mentioning that the s- and p-polarized spectra do not overlap each other. This lack of overlap means the switching range can span from 0.20 to 1.40 THz depending on the deformation of the device along the x - or y -axis direction at incident s- or p-polarized waves. Such a wide switching range for the PSM device allows for potential use in THz-electronic applications with high flexibility and high tunability.

The switching characteristics of the PSM device at incident s- and p-polarized waves are shown in Figure 8 according to the results of Figure 7. The multifunctional states of the PSM device determined by the mechanical inputs (w and l values) are represented by binary digits, where the electromagnetic response of the PSM device with a resonance corresponds to the binary “1” and that without a resonance corresponds to

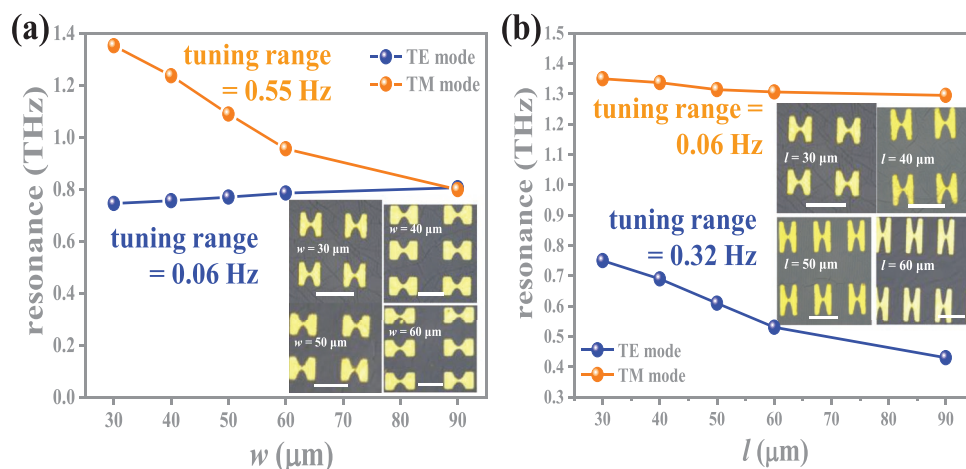


Figure 6. Experimental results and optical microscope images of a PSM device stretched with different a) w and b) l values in the TE and TM modes. Inserted scale bars are 50 μm .

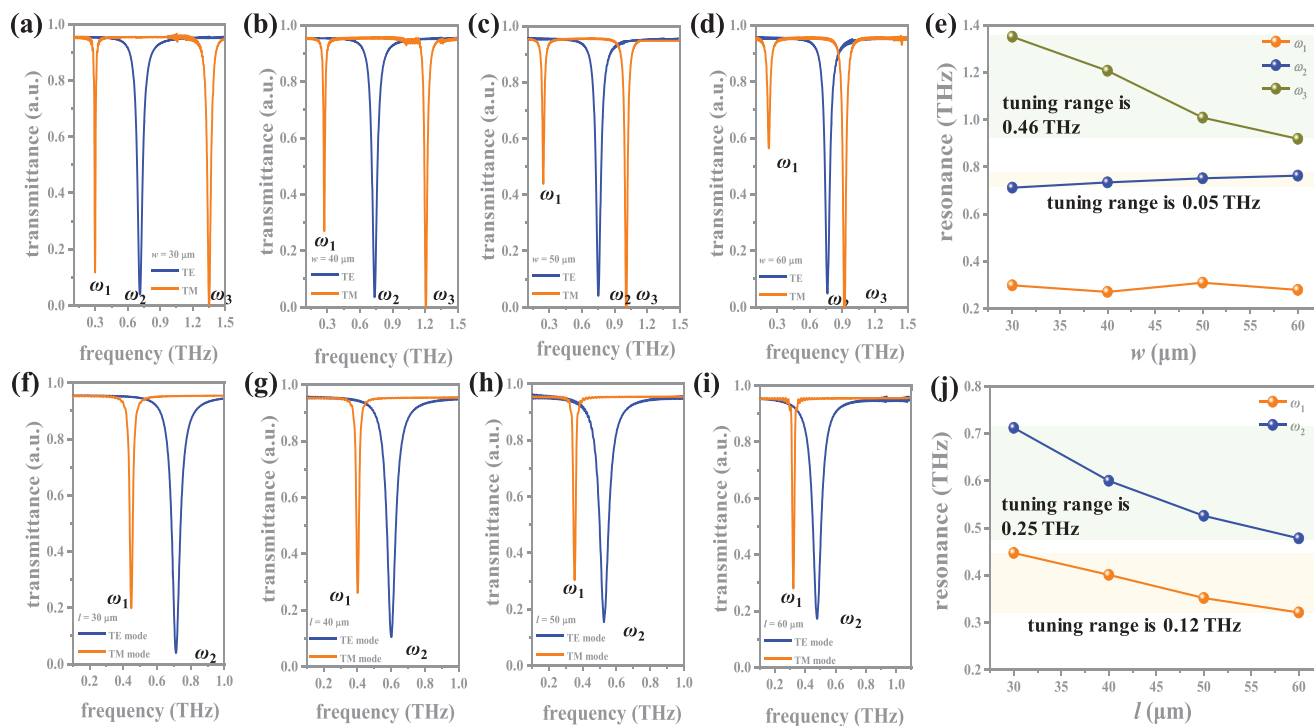


Figure 7. Experimental results for a PSM device stretched with different a–d) w values and f–i) l values in the TE and TM modes. e, j) Summaries for the resonance trends with respect to the variable w and l values, respectively.

binary “0.” The resonance of the PSM device can be switched by an incident s-polarization wave or p-polarization wave denoted as a “1” or “0” digital signal under the same mechanical parameters. Furthermore, the switching characteristics of the PSM device can also be tuned to different resonant frequencies by using mechanical deformation, such as stretching the w and l values to make the digital signal “1” or “0.” The optical tuning range can span from 0.20 to 1.40 THz. Such optical-mechanical behavior indicates that the proposed PSM device can possess multifunctionalities and provides for the possibility of use for active sensors, optics digital processing, nonlinear devices, and modulators in the THz-frequency range.

In summary, we demonstrate a flexible PSM device with an active high-efficiency tunability, large tuning range, and ultrahigh Q -factor. The PSM device exhibits a tunable single- and dual-resonance with ultranarrow bandwidth. These resonances can be tuned by using mechanical force to deform the

geometrical period of the PSM. The resonant tuning range can span from 0.20 to 1.40 THz. The highest Q -factor obtained is 50 for the case of $l = 60 \mu\text{m}$ in the TM mode. In the TE mode, Q -factors for the PSM device with different deformation values for a , b , w , and l are stable and kept in the range of 9 to 14. The PSM device can be used to not only realize an ultranarrowband filter but also a polarization switch in the THz-frequency range. Furthermore, the PSM device exhibits the multifunctionalities of single-/dual-band switching and polarization switching. The integration of the PSM device on a mechanically flexible PDMS substrate offers a new route toward optoelectronics applications and provides potential possibilities for the next generation of programmable and digital metamaterials with multichannel data processing. The demonstrated stretchable THz PSM device possesses high flexibility, applicability, and cost-effectiveness for widespread THz-wave applications.

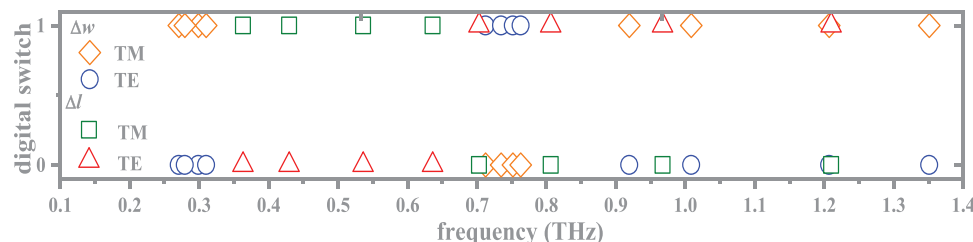


Figure 8. Switching characteristics of the PSM device. The PSM device can be switched to (0, 1) and (1, 0) digital signals by operating at different polarization modes and switched to (0, 0) and (1, 1) digital signals by deforming the device along the x- and y-axes.

Experimental Section

Simulations: The full-field simulated electromagnetic waves were determined by using commercial finite-difference time-domain (FDTD) solutions. The FDTD method was utilized to analyze the optical performance of the proposed PSM device. The boundary conditions were defined as a perfectly matched layer (PML) in the z direction and periodic conditions in the x and y directions. The incident electromagnetic wave was propagated along the z -axis direction in the numerical simulations. The s - and p -polarization waves were defined as the incident electromagnetic wave perpendicular to the x - y plane by setting the E -field along the x -axis direction (i.e., the direction of the PSM width) and along the y -axis direction (i.e., the direction of the PSM length), respectively.

Fabrication: The fabrication process of the PSM device is illustrated as follows. First, a prepared silicon (Si) mold was coated with a SU-8 layer and exposed to chlorotrimethylsilane vapor for 3 min. This sample was baked for 15 min and then released. Second, the prepolymer (RTV615A) and curing agent (RTV615B) for PDMS were mixed in a ratio of 10:1 and then poured onto the mold. Third, the sample was degassed and baked at 85 °C for 30 and 45 min, respectively. Fourth, the desired PDMS sample surface was cleaned using an O_2 plasma to facilitate easy Au-layer adhesion onto the PDMS surface. Fifth, a photoresist on the PDMS surface was patterned by using a photolithography technique, and an Au layer was sequentially deposited onto the PDMS surface by using an electron-beam evaporator. The thickness of the Au layer was 100 nm. Finally, the patterning of the PSM was realized by using a lift-off process followed by peeling off the PDMS substrate with the PSM pattern from the Si mold.

Measurement: The effect of strain on the resonant frequency of the PSM device was experimentally explored by applying an increasing stretched force to deform the PSM along the x - and y -axis directions, respectively. The tested PSM device was mounted onto a test jig. One side of the test PSM device was movable and the other side was fixed. This test jig was connected to a stepper motor, which could be precisely controlled by an electrical input to stretch the PSM device. The testing setup is illustrated in Figure S2 (see the Supporting Information). The PSM device mounted on the test jig was connected to a dc power supply and placed in the chamber of the measurement system. This measurement system was filled with nitrogen gas to eliminate water vapor in the testing chamber. The transmittance of the PSM device was measured by using a commercial THz time-domain spectroscopy system (Teraview 3000). All measured spectra were normalized with respect to the transmittance of a pure PDMS substrate used as a test sample.

Supporting Information

Supporting Information is available from the Wiley Online Library or from the author.

Acknowledgements

The authors acknowledge financial support from the research grants of the 100 Talents Program of Sun Yat-Sen University (Grant No. 76120-18831103), and the State Key Laboratory of Optoelectronic Materials and Technologies of Sun Yat-Sen University for the use of experimental equipment.

Conflict of Interest

The authors declare no conflict of interest.

Keywords

active metamaterials, flexible modulators, multifunctional switches, terahertz devices

Received: March 3, 2019

Revised: May 23, 2019

Published online:

- [1] C. R. Simovski, P. A. Belov, A. V. Atrashchenko, Y. S. Kivshar, *Adv. Mater.* **2012**, 24, 4229.
- [2] M. Lee, H. E. Katz, C. Erben, D. M. Gill, P. Gopalan, J. D. Heber, D. J. McGee, *Science* **2002**, 298, 1401.
- [3] P. Sookchoo, F. F. Sudradjat, A. M. Kiefer, H. Durmaz, R. Paiella, M. G. Lagally, *ACS Nano* **2013**, 7, 2326.
- [4] D. R. Smith, J. B. Pendry, M. C. K. Wiltshire, *Science* **2004**, 305, 788.
- [5] C. L. Yu, H. Kim, N. de Leon, I. W. Frank, J. T. Robinson, M. McCutcheon, M. Liu, M. D. Lukin, M. Loncar, H. Park, *Nano Lett.* **2013**, 13, 248.
- [6] X. Hu, J. Li, X. Wei, *Opt. Express* **2017**, 25, 29617.
- [7] O. Y. Yermakov, A. A. Hurshkainen, D. A. Dobrykh, P. V. Kapitanova, I. V. Iorsh, S. B. Glybovski, A. A. Bogdanov, *Phys. Rev. B* **2018**, 98, 195404.
- [8] V. M. Shalae, *Nat. Photonics* **2007**, 1, 41.
- [9] J. Valentine, S. Zhang, T. Zentgraf, E. Ulin-Avila, D. A. Genov, G. Bartal, X. Zhang, *Nature* **2008**, 455, 376.
- [10] M. Choi, S. H. Lee, Y. Kim, S. B. Kang, J. Shin, M. H. Kwak, K. Y. Kang, Y. H. Lee, N. Park, B. Min, *Nature* **2011**, 470, 369.
- [11] M. J. Smith, S. T. Malak, J. Jung, Y. J. Yoon, C. H. Lin, S. Kim, K. M. Lee, R. Ma, T. J. White, T. J. Bunning, Z. Lin, V. V. Tsukruk, *ACS Appl. Mater. Interfaces* **2017**, 9, 17435.
- [12] S. Misra, L. Li, J. Jian, J. Huang, X. Wang, D. Zemlyanov, J. W. Jang, F. H. Ribeiro, H. Wang, *ACS Appl. Mater. Interfaces* **2018**, 10, 32895.
- [13] D. M. Wu, M. L. Solomon, G. V. Naik, A. Garcia-Etxarri, M. Lawrence, A. Salleo, J. A. Dionne, *Adv. Mater.* **2018**, 30, 1703912.
- [14] C. Yuan, X. Mu, C. K. Dunn, J. Haidar, T. Wang, H. J. Qi, *Adv. Funct. Mater.* **2018**, 28, 1705727.
- [15] B. J. Roxworthy, V. A. Aksyuk, *Optica* **2018**, 5, 71.
- [16] P. Cheben, R. Halir, J. H. Schmid, H. A. Atwater, D. R. Smith, *Nature* **2018**, 560, 565.
- [17] L. Huang, C.-C. Chang, B. Zeng, J. Nogan, S.-N. Luo, A. J. Taylor, A. K. Azad, H.-T. Chen, *ACS Photonics* **2017**, 4, 2111.
- [18] Q. Zhou, P. Liu, L.-a. Bian, H. Liu, C. Liu, G. Chen, *Opt. Commun.* **2018**, 413, 310.
- [19] L. Yang, F. Fan, M. Chen, X. Zhang, S.-J. Chang, *Opt. Commun.* **2017**, 382, 42.
- [20] W. Dong, Y. Qiu, X. Zhou, A. Banas, K. Banas, M. B. H. Breese, T. Cao, R. E. Simpson, *Adv. Opt. Mater.* **2018**, 6, 1701346.
- [21] R. Singh, A. K. Azad, Q. X. Jia, A. J. Taylor, H.-T. Chen, *Opt. Lett.* **2011**, 36, 1230.
- [22] C. H. Kodama, R. A. Couto Jr., *Appl. Phys. Lett.* **2016**, 108, 231901.
- [23] P. Pitchappa, M. Manjappa, H. N. S. Krishnamoorthy, Y. Chang, C. Lee, R. Singh, *Appl. Phys. Lett.* **2017**, 111, 261101.
- [24] P. Pitchappa, C. P. Ho, L. Cong, R. Singh, N. Singh, C. Lee, *Adv. Opt. Mater.* **2016**, 4, 391.
- [25] J. Bauer, L. R. Meza, T. A. Schaedler, R. Schwaiger, X. Zheng, L. Valdevit, *Adv. Mater.* **2017**, 29, 1701850.
- [26] K. Shih, P. Pitchappa, M. Manjappa, C. P. Ho, R. Singh, C. Lee, *J. Appl. Phys.* **2017**, 121, 023102.
- [27] C. P. Ho, P. Pitchappa, C. Lee, *J. Appl. Phys.* **2016**, 119, 153104.
- [28] L. Cong, P. Pitchappa, C. Lee, R. Singh, *Adv. Mater.* **2017**, 29, 1700733.

- [29] K. Shih, P. Pitchappa, M. Manjappa, C. P. Ho, R. Singh, B. Yang, N. Singh, C. Lee, *Appl. Phys. Lett.* **2017**, *110*, 161108.
- [30] M. Manjappa, P. Pitchappa, N. Wang, C. Lee, R. Singh, *Adv. Opt. Mater.* **2018**, *6*, 1800141.
- [31] Q. Xie, G. X. Dong, B. X. Wang, W. Q. Huang, *Nanoscale Res. Lett.* **2018**, *13*, 294.
- [32] S. Khan, T. F. Eibert, *IEEE Trans. Antennas Propag.* **2018**, *66*, 4042.
- [33] L.-P. Sun, X. Zhai, Q. Lin, G.-D. Liu, L.-L. Wang, *Plasmonics* **2018**, *13*, 1043.
- [34] H. I. Lin, K. C. Shen, S. Y. Lin, G. Haider, Y. H. Li, S. W. Chang, Y. F. Chen, *Sci. Rep.* **2018**, *8*, 9469.
- [35] P. Gutruf, C. Zou, W. Withayachumnankul, M. Bhaskaran, S. Sriram, C. Fumeaux, *ACS Nano* **2016**, *10*, 133.
- [36] K. Shih, P. Pitchappa, L. Jin, C.-H. Chen, R. Singh, C. Lee, *Appl. Phys. Lett.* **2018**, *113*, 071105.
- [37] M. Manjappa, P. Pitchappa, N. Singh, N. Wang, N. I. Zheludev, C. Lee, R. Singh, *Nat. Commun.* **2018**, *9*, 4056.
- [38] Z. Zhou, T. Zhou, S. Zhang, Z. Shi, Y. Chen, W. Wan, X. Li, X. Chen, S. N. G. Corder, Z. Fu, L. Chen, Y. Mao, J. Cao, F. G. Omenetto, M. Liu, H. Li, T. H. Tao, *Adv. Sci.* **2018**, *5*, 1700982.
- [39] M. Manjappa, Y. K. Srivastava, L. Cong, I. Al-Naib, R. Singh, *Adv. Mater.* **2017**, *29*, 1603355.
- [40] K. Fan, H. Y. Hwang, M. Liu, A. C. Strikwerda, A. Sternbach, J. Zhang, X. Zhao, X. Zhang, K. A. Nelson, R. D. Averitt, *Phys. Rev. Lett.* **2013**, *110*, 217404.
- [41] A. Benz, M. Krall, S. Schwarz, D. Dietze, H. Detz, A. M. Andrews, W. Schrenk, G. Strasser, K. Unterrainer, *Sci. Rep.* **2015**, *4*, 4269.
- [42] S. Alfihed, M. H. Bergen, J. F. Holzman, I. G. Foulds, *Polymer* **2018**, *153*, 325.
- [43] P. Klonos, Y. Bolbukh, C. S. Koutsira, K. Zafeiris, O. D. Kalogeri, D. Sternik, A. Derylo-Marczewska, V. Tertykh, P. Pissis, *Polymer* **2018**, *148*, 1.
- [44] S. B. Iyer, A. Dube, N. M. Dube, P. Roy, R. R. N. Sailaja, *J. Mech. Behav. Biomed. Mater.* **2018**, *86*, 23.
- [45] D. Morits, M. Morits, V. Ovchinnikov, M. Omelyanovich, A. Tamminen, S. Tretyakov, C. Simovski, *J. Opt.* **2014**, *16*, 032001.
- [46] K. Kim, D. Lee, S. Eom, S. Lim, *Sensors* **2016**, *16*, 521.
- [47] X. P. Zhang, J. Zhang, H. M. Liu, X. Q. Su, L. Wang, *Sci. Rep.* **2014**, *4*, 6.
- [48] P. Zhou, L. Wang, G. Zhang, J. Jiang, H. Chen, Y. Zhou, D. Liang, L. Deng, *IEEE Trans. Antennas Propag.* **2019**, *67*, 291.
- [49] F. L. Zhang, S. Q. Feng, K. P. Qiu, Z. J. Liu, Y. C. Fan, W. H. Zhang, Q. Zhao, J. Zhou, *Appl. Phys. Lett.* **2015**, *106*, 091907.
- [50] M. D. Dickey, *Adv. Mater.* **2017**, *29*, 1606425.
- [51] P. Pitchappa, C. P. Ho, L. Dhakar, C. Lee, *Optica* **2015**, *2*, 571.
- [52] X.-J. Shang, X. Zhai, J. Yue, X. Luo, J.-P. Liu, X. P. Zhu, H. G. Duan, L.-L. Wang, *Opt. Express* **2017**, *25*, 14406.
- [53] I. Koirala, V. R. Shrestha, C.-S. Park, S. Gao, S.-S. Lee, D.-Y. Choi, *Sci. Rep.* **2017**, *7*, 13574.
- [54] X. Chen, T. M. Grzegorzczak, B.-I. Wu, J. Pacheco Jr., J. A. Kong, *Phys. Rev. E* **2004**, *70*, 016608.
- [55] D. R. Smith, S. Schultz, P. Markos, C. M. Soukoulis, *Phys. Rev. B* **2002**, *65*, 195104.
- [56] Z. Vafapour, *Appl. Opt.* **2018**, *57*, 722.
- [57] J. Paulose, B. G.-g. Chen, V. Vitelli, *Nat. Phys.* **2015**, *11*, 153.
- [58] W. Zhu, R. S. Yang, Y. C. Fan, Q. H. Fu, H. J. Wu, P. Zhang, N. H. Shenb, F. Zhang, *Nanoscale* **2018**, *10*, 12054.
- [59] S.-E. Mun, H. Yun, C. Choi, S.-J. Kim, B. Lee, *Adv. Opt. Mater.* **2018**, *6*, 1800545.
- [60] T. A. Elwi, *Int. J. RF Microwave Comput.-Aided Eng.* **2018**, *28*, e21470.